Actin-binding protein G (AbpG) participates in modulating the actin cytoskeleton and cell migration in *Dictyostelium discoideum*

Wei-Chi Lin[a], Liang-Chen Wang[a], Te-Ling Pang[a,*], and Mei-Yu Chen[a,b]
[a]Institute of Biochemistry and Molecular Biology and [b]Genome Research Center, National Yang-Ming University, Taipei 11221, Taiwan

ABSTRACT **Cell migration is involved in various physiological and pathogenic events, and the complex underlying molecular mechanisms have not been fully elucidated. The simple eukaryote *Dictyostelium discoideum* displays chemotactic locomotion in stages of its life cycle. By characterizing a *Dictyostelium* mutant defective in chemotactic responses, we identified a novel actin-binding protein serving to modulate cell migration and named it actin-binding protein G (AbpG); this 971–amino acid (aa) protein contains an N-terminal type 2 calponin homology (CH2) domain followed by two large coiled-coil regions. In chemoattractant gradients, *abpG*$^-$ cells display normal directional persistence but migrate significantly more slowly than wild-type cells; expressing Flag-AbpG in mutant cells eliminates the motility defect. AbpG is enriched in cortical/lamellipodial regions and colocalizes well with F-actin; aa 401–600 and aa 501–550 fragments of AbpG show the same distribution as full-length AbpG. The aa 501–550 region of AbpG, which is essential for AbpG to localize to lamellipodia and to rescue the phenotype of *abpG*$^-$ cells, is sufficient for binding to F-actin and represents a novel actin-binding protein domain. Compared with wild-type cells, *abpG*$^-$ cells have significantly higher F-actin levels. Collectively our results suggest that AbpG may participate in modulating actin dynamics to optimize cell locomotion.**

Monitoring Editor
Carole Parent
National Institutes of Health

Received: May 13, 2014
Revised: Jan 12, 2015
Accepted: Jan 14, 2015

INTRODUCTION

In various physiological and pathological events, such as embryonic development, inflammatory and immune responses, and cancer metastasis, cell migration responding to environmental cues is a pivotal mechanism (Bravo-Cordero *et al.*, 2012; Solnica-Krezel and Sepich, 2012; Kolaczkowska and Kubes, 2013). The migration process requires the coordination of signaling pathways and the motility machinery (Insall, 2013), and the complex underlying molecular network remains to be fully elucidated.

Eukaryotic cell migration generally involves drastic cell shape changes driven by the rearrangement of cytoskeleton. In the crawling movement of cells, continuous reorganization and turnover of the actin cytoskeleton occur (Pollard and Borisy, 2003). At the cell front, rapid actin polymerization drives the extension of membrane protrusions such as lamellipodia and filopodia (Bisi *et al.*, 2013). The new cellular protrusions adhere to the substratum through proteins that can engage the extracellular matrix to provide anchor points. For optimal migratory movement, a cell needs the contraction ability to drive the translocation of the trailing cell body; this ability depends on the interaction between actin filaments and myosin (Cramer, 2013). The cell rear is detached from the original adhesion to allow the cell to advance a step. These events proceed in a cyclical manner and are spatially and temporally coordinated (Lauffenburger and Horwitz, 1996; Maruthamuthu *et al.*, 2010).

Dynamic reorganization of the actin cytoskeleton is intricately controlled by a myriad of actin-binding proteins (ABPs; Winder and Ayscough, 2005). Two forms of actin—globular monomeric G-actin

This article was published online ahead of print in MBoC in Press (http://www.molbiolcell.org/cgi/doi/10.1091/mbc.E14-05-0972) on January 21, 2015.

*Present address: Vectorite Biomedical, Taipei 10586, Taiwan.

Address correspondence to: Mei-Yu Chen (meychen@ym.edu.tw).

Abbreviations used: ABP, actin-binding protein; AbpG, actin-binding protein G; cAMP, 3′-5′-cyclic adenosine monophosphate; CH, calponin homology; CRAC, cytosolic regulator of adenylyl cyclase; GST, glutathione *S*-transferase; PtdIns(3,4,5)P_3, phosphatidylinositol (3,4,5)-triphosphate; REMI, restriction enzyme–mediated integration.

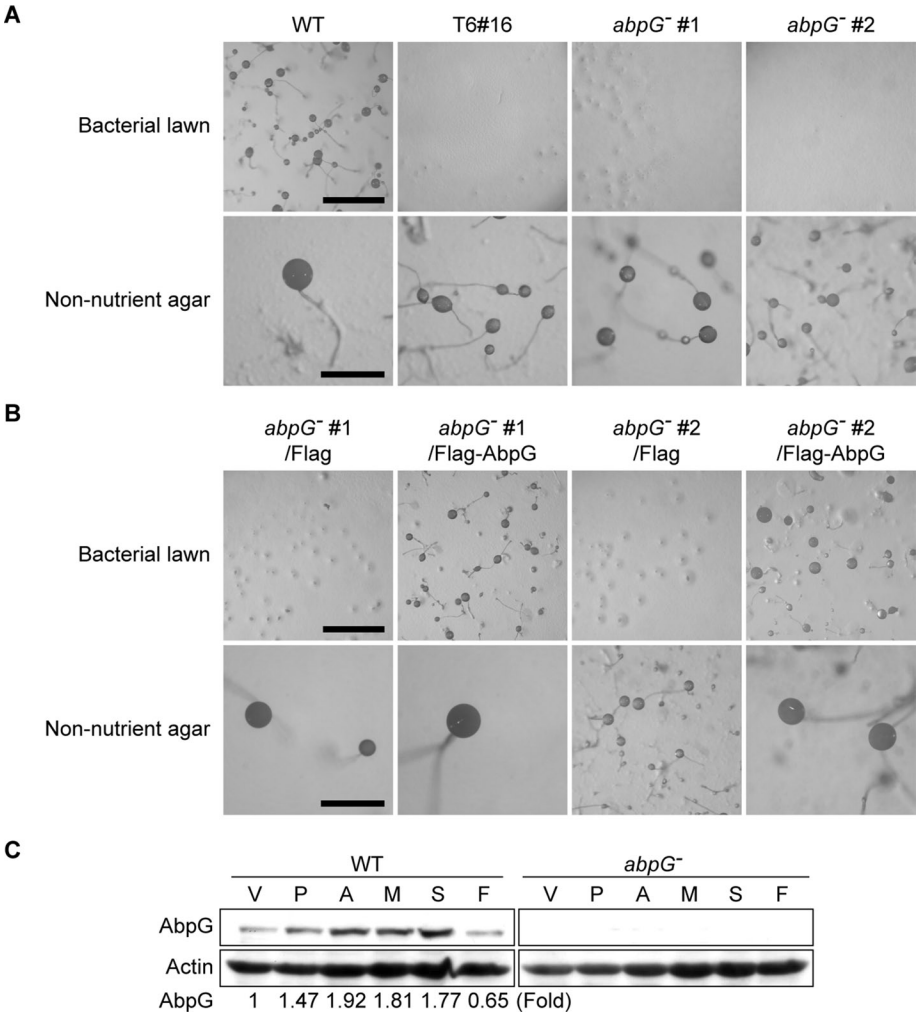

FIGURE 1: Aberrant developmental morphology of cells with disrupted *abpG*.
(A, B) Developmental phenotype. Cells developed on bacterial lawns and non-nutrient agar were photographed 5–7 d and 24–36 h, respectively, after plating. Bars, 2 mm (bacterial lawn), 500 µm (non-nutrient agar). (C) AbpG expression during development. Cells were developed on non-nutrient agar and harvested at different time points. Total lysates were analyzed by Western blotting with antibodies against AbpG and actin. Relative AbpG levels (normalized to actin and relative to the value in V) are shown at the bottom. A, aggregation; F, fruiting body; M, mound; P, preaggregation; S, slug; V, vegetative.

and filamentous polymeric F-actin—coexist in cells in a dynamic equilibrium; ATP–G-actin monomers add to the barbed end, and ADP–G-actin subunits dissociate from the pointed end of F-actin. The released ADP–G-actin monomers undergo nucleotide exchange to replenish the cellular ATP–G-actin pool for new rounds of actin filament assembly. Many ABPs have been identified and categorized into a few major families based on the actin-binding domains, including the actin-depolymerizing factor homology (ADF-H) domain, the gelsolin homology domain, the Wiskott–Aldrich syndrome protein (WASP) homology-2 (WH2) domain, the calponin homology (CH) domain, and the myosin motor domain (Paunola *et al.*, 2002; McGough *et al.*, 2003; Disanza *et al.*, 2005; Friedberg and Rivero, 2010; Poukkula *et al.*, 2011; Hartman and Spudich, 2012). ABPs can associate with G-actin and/or F-actin and regulate the actin cytoskeleton in different ways (Winder and Ayscough, 2005). For example, the Arp2/3 complex binds to actin and serves as a nucleation factor to promote branching of the filaments (Machesky *et al.*, 1997; Machesky and Insall, 1998). The ADF/cofilin family members are disassembly factors with filament-severing activities (Prochniewicz *et al.*, 2005). Other activities of ABPs include filament capping, debranching, monomer binding, bundling, and cross-linking (Winder and Ayscough, 2005). The repertoire of actin regulators is still expanding, and the cellular roles of many ABPs are still elusive.

Dictyostelium discoideum is a simple eukaryote that exhibits chemotactic migration in multiple stages of its life cycle. During growth, *Dictyostelium* amoebae migrate toward bacteria and consume them by phagocytosis as their food. Under nutrient depletion, *Dictyostelium* cells enter a developmental program in which single cells collectively move toward the cAMP signals released from designated central cells, forming aggregates that later undergo differentiation and morphogenesis to turn into multicellular structures (Kay, 2002; Weijer, 2009). With the many available molecular genetics tools and the haploid state ideal for genetic screening, *Dictyostelium* has been extensively exploited in studying cell migration and actin regulation (Egelhoff and Spudich, 1991; Noegel and Schleicher, 2000).

To uncover novel molecular players in the pathways underlying chemotactic cell migration, we previously performed a screen for *Dictyostelium* mutants defective in chemotactic responses to cAMP (Pang *et al.*, 2010). In the present study, we analyzed a mutant collected in the screen and identified a novel actin-binding protein involved in modulating cell migration.

RESULTS

Identification of the *abpG* gene

T6#16 was a restriction enzyme–mediated integration (REMI)–generated mutant that showed defective chemotactic movement. Through standard REMI plasmid recovery procedures and sequencing analysis, we identified DDB0185522, a previously uncharacterized open reading frame located at coordinates 702819–705881 of chromosome 4, as the gene disrupted in T6#16. We named this gene *abpG* and its 971–amino acid (aa) product actin-binding protein G (AbpG) (see later discussion). We engineered another mutant allele (*abpG*⁻) by replacing part of the *abpG* coding sequence with a selection marker expression cassette (Supplemental Figure S1). T6#16 and two independent *abpG*⁻ clones displayed similar developmental morphology, producing smooth plaques on bacteria lawns and smaller-than-wild-type fruiting bodies on non-nutrient agar (Figure 1A); the mutant phenotype of *abpG*⁻ cells could be rescued by expressing Flag-AbpG (Figure 1B), indicating that the abnormality was caused by lack of functional AbpG. We examined the expression of *abpG* during development and found that AbpG protein levels peaked at the aggregation stage (Figure 1C), which is consistent with a possible role of AbpG in supporting chemotactic migration.

The migration phenotype of *abpG*⁻ cells

We examined the chemotactic response of cells lacking AbpG in semiquantitative small-drop chemotaxis assays. T6#16 and two independent *abpG*⁻ clones responded to the same range of cAMP concentrations as did wild-type cells, with a peak response at 10^{-7} M, although the responses were significantly less efficient (Figure 2A).

We further performed micropipette chemotaxis assays and recorded the migratory behavior of cells in cAMP gradients by time-lapse video microscopy. At 20 min after being exposed to a micropipette releasing cAMP, many wild-type cells had reached the tip of micropipette, whereas T6#16 and *abpG*⁻ cells failed to display a robust response (Figure 2B and Supplemental Movies S1–S3). We tracked the migration of individual cells and found that although T6#16 and *abpG*⁻ cells still moved toward the chemoattractant source, they displayed shorter migrating tracks than the wild-type cells (Figure 2B). The average migration speed of T6#16 or *abpG*⁻ cells was significantly lower than that of wild-type cells; however, parameters for migration directionality, including directional persistence and chemotaxis index, were similar in wild-type and mutant cells (Table 1). Expressing Flag-AbpG in *abpG*⁻ cells was able to eliminate the motility defect (Figure 2C and Supplemental Movies S4 and S5); compared with *abpG*⁻ cells transformed with the control vector, Flag-AbpG–expressing *abpG*⁻ cells displayed longer migration tracks and a higher migration speed (Figure 2C and Table 1). We also recorded and analyzed the random migration of vegetative cells of different strains; the results showed that *abpG*⁻ cells migrated at an average speed (2.53 ± 0.45 μm/min) significantly lower than that of the wild-type cells (3.75 ± 0.99 μm/min). Together our data suggest that AbpG functions to support optimal cell migration.

A direction-sensing mechanism in *Dictyostelium* involves the asymmetrical activation of phosphatidylinositide 3-kinase to generate a local surge of phosphatidylinositol (3,4,5)-triphosphate (PtdIns(3,4,5)P_3; Funamoto *et al.*, 2002). PH_{CRAC}-GFP, which is the pleckstrin homology (PH) domain from cytosolic regulator of adenylyl cyclase (CRAC) fused to the green fluorescence protein (GFP) marker, can be directed to PtdIns(3,4,5)P_3-rich membrane locations (Insall *et al.*, 1994). We used PH_{CRAC}-GFP as a probe for PtdIns(3,4,5)P_3 and found that in both wild-type and *abpG*⁻ cells, PH_{CRAC}-GFP signals appeared at the leading edge while cells were migrating in the gradient of cAMP (Supplemental Figure S2A and Supplemental Movies S6 and S7). On uniform cAMP stimulation, *abpG*⁻ cells displayed similar kinetics of PH_{CRAC}-GFP membrane translocation to that observed in wild-type cells, with the cytosolic PH_{CRAC}-GFP signals decreased and the membrane PH_{CRAC}-GFP signals increased at 4 s after cAMP stimulation (Supplemental Figure S2B). These data indicated that the PtdIns(3,4,5)P_3-based directional sensing mechanism was not affected in *abpG*⁻ cells, consistent with their wild-type-like directionality shown in Table 1.

We analyzed the morphology of *abpG*⁻ cells during chemotactic migration by performing time-lapse video microscopy at high magnification in the micropipette assay. In the cAMP gradient, compared with wild-type/GFP cells, which spread out to an elongated shape and moved efficiently toward the cAMP, *abpG*⁻/GFP cells were less elongated and migrated significantly more slowly (Figure 2D and Supplemental Movies S8 and S9). The average length/width ratio of *abpG*⁻ cells during cell migration was significantly smaller than that of wild-type cells.

Distribution of AbpG in cells

Given the reduced motility and the less-elongated shape of *abpG*⁻ cells in chemotaxis, we speculated that AbpG may participate in

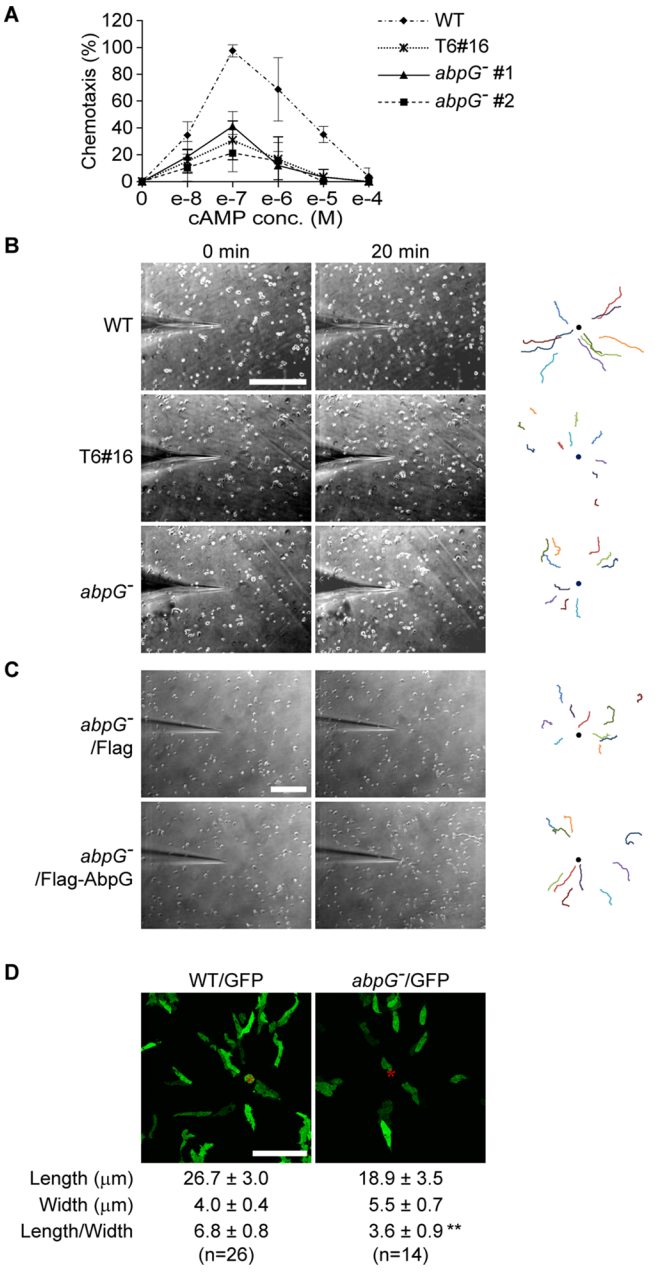

FIGURE 2: Abnormal chemotactic migration in cells with disrupted *abpG*. Cells were developed for 5–6 h with cAMP pulsing to become aggregation competent. (A) Small-drop chemotaxis assay. Developed cells in small drops were placed adjacent to cAMP drops on agar and examined after 20 min. Drops showing more cells on the cAMP side were scored positive for chemotaxis. Shown are the percentages (mean ± SD) of positive drops for each cAMP concentration obtained from three independent experiments. (B, C) Micropipette chemotaxis assay. Cells were stimulated with cAMP released from a Femtotip. Images were captured every 10 s for a period of 20 min. Shown are micrographs taken before (0 min) and after (20 min) cAMP stimulation. Migration tracks of 10 cell centroids are shown on the right; black dot, the position of the Femtotip. Bar, 200 μm. (D) Morphology of migrating cells. Images of developed GFP-expressing wild-type (WT) or *abpG*⁻ cells migrating in the micropipette cAMP chemotaxis assay were taken under a confocal microscope. Red asterisk, the position of Femtotip. Bar, 50 μm. Actual lengths and widths of individual cells were measured using MetaMorph software, and the length/width ratio was calculated for each cell; shown below the micrographs are results (mean ± SD) obtained from four independent experiments. $^{**}p < 0.01$.

Strain (n = 30/strain)	Migration speed (μm/min)	Directional persistence	Chemotaxis index
Wild type	8.54 ± 2.12	0.80 ± 0.09	0.73 ± 0.11
T6#16	2.91 ± 0.93*	0.76 ± 0.10	0.72 ± 0.10
abpG$^-$	4.74 ± 1.05*	0.80 ± 0.08	0.74 ± 0.12
abpG$^-$/Flag	6.25 ± 1.64**	0.72 ± 0.11	0.65 ± 0.16
abpG$^-$/Flag-AbpG	8.69 ± 1.33	0.74 ± 0.14	0.66 ± 0.18
abpG$^-$/Flag-AbpGΔ501-550	6.57 ± 1.57**	0.76 ± 0.08	0.66 ± 0.17

Migration speed, migration distance per unit time. Directional persistence, net to total path length. Chemotaxis index, the cosine value of the angle between the direction of cell movement and the direction toward the chemoattractant source. Data presented are means with SDs from three independent experiments; *n*, total number of cells traced.
*$p < 0.01$ (*t* test), compared with wild-type cells; **$p < 0.01$ (*t* test), compared with *abpG*$^-$/Flag-AbpG cells.

TABLE 1: Computer-assisted analysis of cell migration.

regulating the cytoskeleton. Results of Western blot analysis on detergent-soluble and -insoluble fractions of cell lysates showed that a significant amount of AbpG existed in the pellet fraction, consistent with the notion that AbpG can associate with cytoskeletal components (Figure 3A). We investigated the subcellular localization of AbpG by immunofluorescence cell staining. The AbpG-specific antiserum we generated could barely detect endogenous AbpG in immunofluorescence experiments; therefore we used AbpG-overexpressing cells to examine the localization of AbpG. The distribution of Flag-AbpG, which could rescue phenotypes of *abpG*$^-$ cells as mentioned earlier, was enriched at the edge of lamellipodia, colocalizing with signals of F-actin in both vegetative- and aggregative-stage cells (Figure 3B and Supplemental Figure S3A). An N-terminally monomeric red fluorescent protein (mRFP)–tagged AbpG also showed similar cortical/lamellipodial distribution in wild-type and *abpG*$^-$ cells (Supplemental Figure S3B). We next checked whether AbpG exhibits dynamic spatial distributions in actively migrating cells. Aggregation-competent wild-type cells coexpressing mRFP-AbpG and LifeAct-GFP (which specifically labels F-actin) were subjected to the micropipette cAMP chemotaxis assay and time-lapse video microscopy. Analysis of fluorescence signals in micrographs revealed that the appearance of mRFP-AbpG and the assembly of F-actin at the leading edge during migration shared similar kinetics (Figure 3C). Note that AbpG could localize to locations other than the leading edge. When we analyzed micrographs obtained from time-lapse video microscopy in Figure 3C and quantitated the fluorescence signals of mRFP-AbpG and LifeAct-GFP along the long axis of cell, the results showed that AbpG could also colocalize with F-actin at the rear of cells (Supplemental Figure S3C). Together our data highlight the spatial and temporal colocalization of AbpG with F-actin in migrating cells.

We investigated the region of AbpG protein that is required for its cortical/lamellipodial localization. SMART analysis (http://smart.embl-heidelberg.de/; Schultz *et al.*, 1998) on the AbpG sequence revealed a predicted type 2 calponin homology (CH2) domain in the N-terminal region (aa 7–117), which was followed by two large coiled-coil regions. On the basis of this predicted domain structure, we prepared plasmids to express a series of AbpG fragments that are fused with mRFP at their N-termini (Figure 4A) and assessed the cellular distribution of these mRFP-AbpG fragments in vegetative wild-type cells (Figure 4B). Among the AbpG N-terminal truncations, mRFP-AbpG(152-971) and mRFP-AbpG(401-971) exhibited a pattern of cortical red fluorescence enriched at cell protrusions similar to that displayed by the full-length mRFP-AbpG, whereas mRFP-AbpG(601-971) lost the cortical distribution and showed a diffuse cytoplasmic fluorescence pattern. Among the C-terminal truncations, mRFP-AbpG(1-750) and mRFP-AbpG(1-600) maintained the characteristic AbpG distribution, whereas mRFP-AbpG(1-400) and mRFP-AbpG(1-159) did not. These data indicated that the CH2 domain is neither necessary nor sufficient for the cortical/lamellipodial distribution and suggested that the region important for AbpG localization is located within aa 401–600. We found mRFP-AbpG(401-600) displaying the same fluorescence pattern as the full-length AbpG. We further dissected the aa 401–600 region; among the fusion proteins of mRFP and four different 50-aa fragments from aa 401–600 of AbpG, only mRFP-AbpG(501-550) distributed similarly as the full-length mRFP-AbpG. In aggregation-competent wild-type cells, the distributions of full-length mRFP-AbpG, mRFP-AbpG(401-600), and mRFP-AbpG(501-550) signals were also enriched at lamellipodia and colocalized well with F-actin (Figure 4C). These results indicate that the aa 501–550 region contains the required element for directing AbpG localization.

Interaction of AbpG with F-actin

Given the colocalization of AbpG and F-actin, we next examined whether AbpG can physically interact with F-actin. We performed immunoprecipitation in lysates from vector-control and Flag-AbpG–expressing wild-type or *abpG*$^-$ cells using a monoclonal anti-Flag antibody. Western analysis on the precipitated proteins demonstrated specific, although not very robust, coimmunoprecipitation of actin with Flag-AbpG (Figure 5A), indicating that AbpG can associate with actin in the context of cells. To map the AbpG region required for interacting with actin, we expressed glutathione *S*-transferase (GST)–fused AbpG aa 1–200, 201–400, 401–600, and 601–971 fragments in wild-type *Dictyostelium* cells; lysates were prepared from aggregation-stage cells and subjected to GST pull-down procedures. Western analysis on the pulled-down proteins showed that only the aa 401–600 AbpG fragment could interact with actin (Figure 5B). Furthermore, we expressed GST fusions to the four 50-aa AbpG fragments within the aa 401–600 region in *Escherichia coli*. These four GST-AbpG fragments were purified and mixed with lysates of aggregative wild-type *Dictyostelium* cells and tested for actin interaction in GST pull-down assays. The results demonstrated that actin was pulled down by GST-AbpG(501-550) but not the other three GST-AbpG fragments (Figure 5C). We checked whether the association of GST-AbpG(501-550) with actin could still occur when the F-actin organization is disrupted. The results showed that

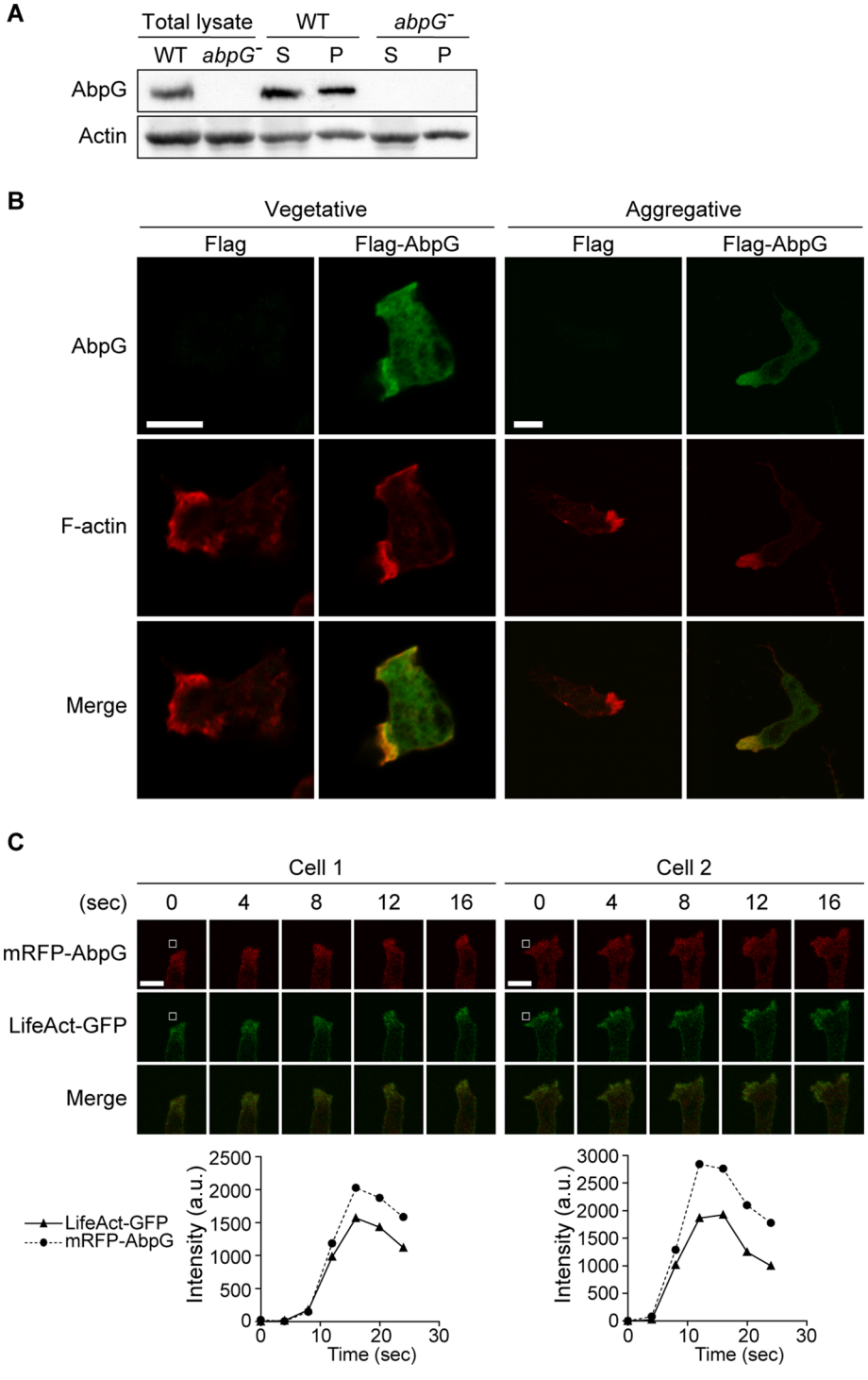

FIGURE 3: Subcellular distribution of AbpG. (A) Localization of AbpG in the detergent-insoluble cytoskeleton. Triton X-100–soluble (S) and –insoluble (P) fractions were prepared from aggregative cells and analyzed by Western blotting using antibodies against AbpG and actin. (B) Colocalization of AbpG and F-actin in fixed cells. Vegetative or aggregative Flag- or Flag-AbpG–expressing *abpG*⁻ cells were fixed and reacted with purified antibodies against N-terminal AbpG and with Phalloidin-TRITC. Bar, 5 μm. (C) Distribution of mRFP-AbpG and F-actin in migrating cells. Wild-type cells transformed to express LifeAct-GFP and mRFP-AbpG were developed and subjected to micropipette assays. Cells were observed under a confocal microscope, and images were taken every 4 s. Two sets of consecutive micrographs are shown. The fluorescence signals of mRFP-AbpG and LifeAct-GFP within a small area at the lamellipodial front (square) were quantified using MetaMorph software; relative intensities (fold) are plotted against time. Bar, 5 μm.

GST-AbpG(501-550) failed to pull down a detectable amount of actin in lysates prepared from cells that were pretreated with latrunculin B (which is a disruptor of microfilament organization; Figure 5D), consistent with the finding from the mRFP-AbpG studies that AbpG colocalized with cortical F-actin. We next used in vitro F-actin sedimentation assays using purified recombinant AbpG fragments to test for direct interaction with F-actin. Whereas GST remained in the supernatant, GST-AbpG(401-600) and GST-AbpG(501-550) primarily cosedimented with F-actin to the pellet fraction like α-actinin (a well-known F-actin–binding protein) did (Figure 5E), indicating that the aa 501–550 region of AbpG is sufficient to mediate direct interaction with F-actin in vitro. In addition, we tested AbpG fragments for G-actin–binding activity by an in vitro G-actin–sequestering assay; G-actin monomers were preincubated with purified recombinant GST-AbpG(401-600) before initiating the polymerization reaction. The results showed that preincubation with GST-AbpG(401-600) did not reduce the level of resulting F-actin (Supplemental Figure S4A), suggesting that AbpG(401-600) does not sequester G-actin monomers.

We further investigated the functional importance of the actin-binding aa 501–550 region of AbpG. We deleted the region corresponding to aa 501–550 of AbpG in GST-AbpG(401-600) and tested the resulting GST-AbpG(401-600)Δ501-550 recombinant protein for direct interaction with actin in the in vitro F-actin sedimentation assay. The results showed that whereas GST-AbpG(401-600) cosedimented efficiently with F-actin to the pellet fraction, a significant amount of GST-AbpG(401-600)Δ501-550 remained in the supernatant after centrifugation in the presence of F-actin (Figure 6A), indicating that the aa 501–550 region is important for efficient interaction with F-actin. We deleted the aa 501–550 region of AbpG in mRFP-AbpG(401-600) and full-length mRFP-AbpG and found that both mRFP-AbpG(401-600)Δ501-550 and mRFP-AbpGΔ501-550 displayed a diffuse red fluorescence pattern (Figure 6B), demonstrating that the 50-aa actin-binding region is required for directing AbpG to cortical/lamellipodial regions. In addition, Flag-AbpGΔ501-550 could not rescue the developmental defect of *abpG*⁻ cells like Flag-AbpG did (Figure 6C), suggesting that the association with cortical F-actin may be important for the cellular function of AbpG.

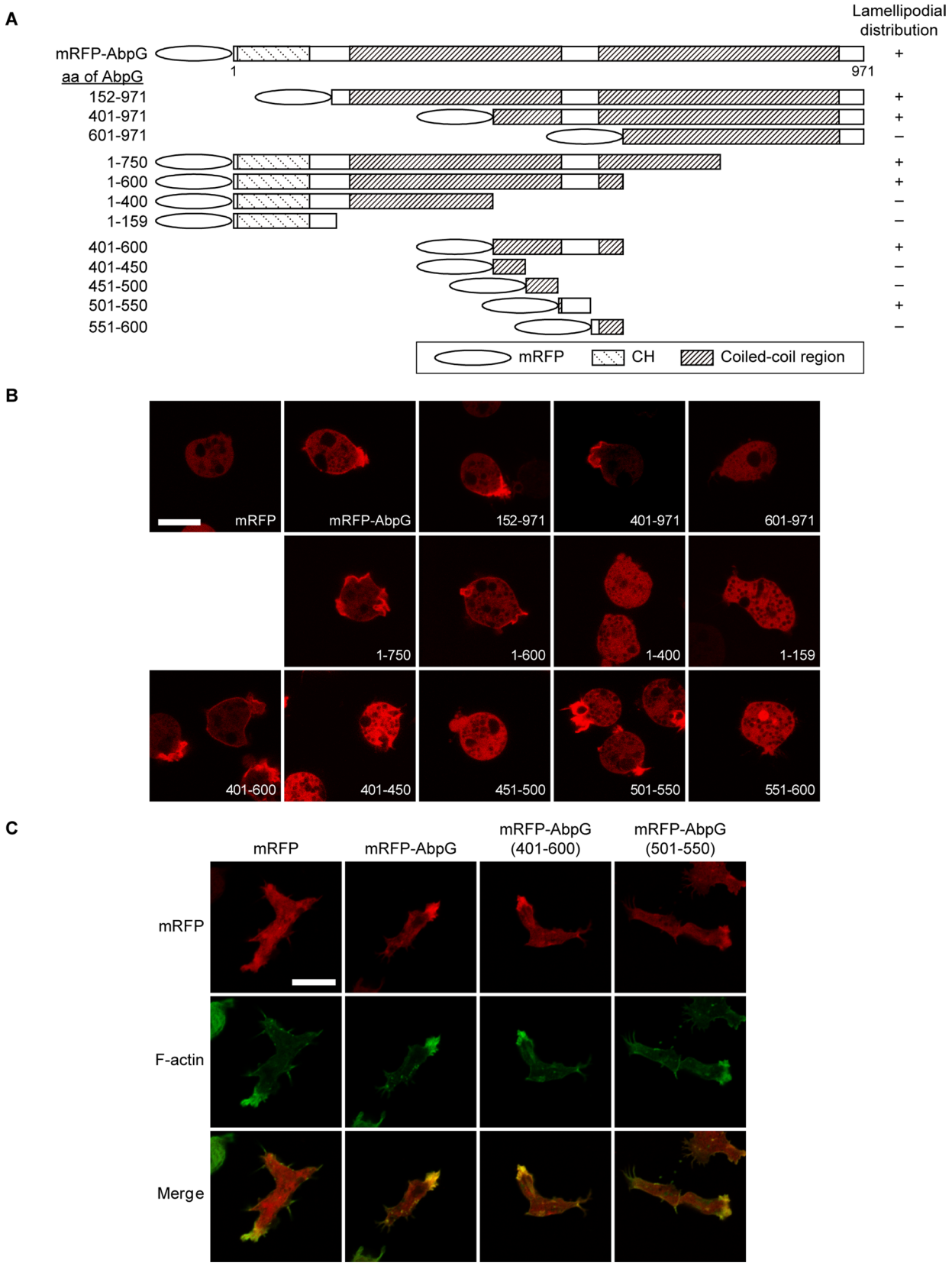

FIGURE 4: Mapping the region required for the cortical/lamellipodial distribution of AbpG. (A) Schematic representation of AbpG protein structure and different AbpG fragments used in domain mapping. (B) Cellular distribution of different AbpG fragments. Live vegetative wild-type cells expressing mRFP or mRFP-AbpG fragments were observed under a confocal fluorescence microscope with a 100× objective. Bar, 10 μm. (C) Colocalization of AbpG fragments and F-actin. Developed wild-type cells expressing mRFP, mRFP-AbpG, mRFP-AbpG(401-600), or mRFP-AbpG(501-550) were fixed and stained with Phalloidin-FITC. Images were taken under a confocal microscope. Bar, 10 μm.

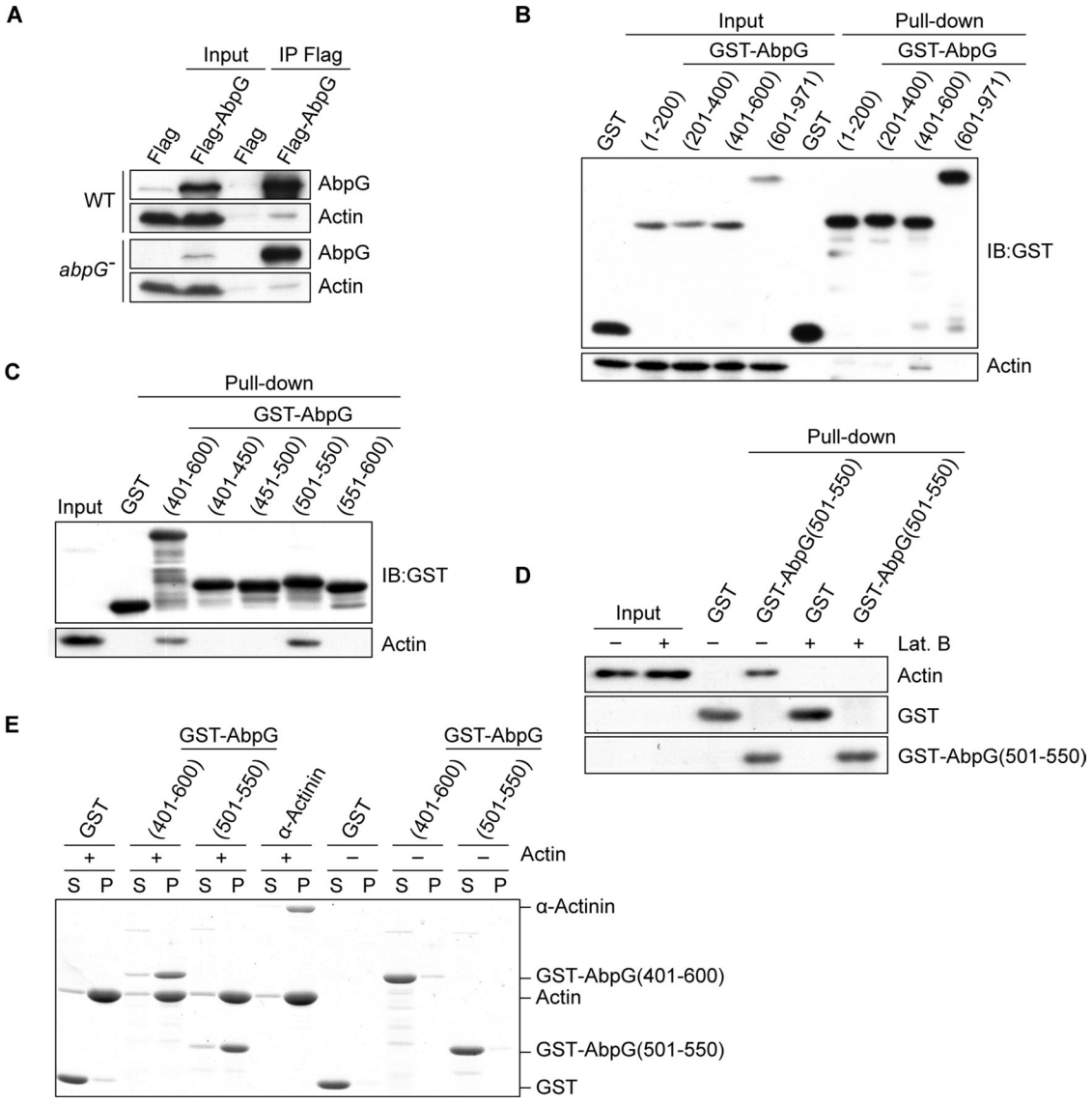

FIGURE 5: Interaction between AbpG and F-actin. (A) Coimmunoprecipitation assay. Lysates from developed Flag- or Flag-AbpG–expressing wild-type or *abpG*⁻ cells were immunoprecipitated using a Flag-specific antibody. Precipitated proteins were analyzed by SDS–PAGE and Western blotting using AbpG and actin antibodies. (B–D) GST pull-down assay. GST-AbpG fragments expressed in developed wild-type *Dictyostelium* cells (B) or recombinant GST-AbpG fragments (purified from *E. coli*) that were mixed with *Dictyostelium* lysates (C, D) were subjected to GST pull-down procedures using glutathione Sepharose beads. *Dictyostelium* lysates were from untreated developed cells (C) or developed cells pretreated with dimethyl sulfoxide or latrunculin B (D). Pulled-down proteins were analyzed using SDS–PAGE, followed by Western blotting. (E) In vitro F-actin sedimentation assay. A GST-AbpG fusion protein (purified from *E. coli*) or α-actinin was added into the polymerization reaction. Reaction mixtures were subsequently centrifuged to sediment F-actin. Supernatant and pellet fractions were analyzed using SDS–PAGE, followed by Coomassie blue staining.

The actin phenotype of *abpG*⁻ cells

We explored the role of AbpG in regulating the actin cytoskeleton using in vitro actin assays. Despite multiple attempts, we were not able to obtain recombinant full-length AbpG using *E. coli* expression systems. We therefore used recombinant AbpG fragments and tested their effects on actin polymerization or F-actin depolymerization in vitro. In the pyrene–actin polymerization assay, as G-actin monomers are polymerized into F-actin, the fluorescence increases and can be monitored in real-time by spectroscopy. Under our experimental conditions, the addition of AbpG(401-600) in the reaction inhibited actin polymerization, whereas adding the same amount of AbpG(501-550) or AbpG(401-600)Δ501-550 did not produce observable effects (Figure 7A). Additional dose–response analysis of in vitro actin polymerization using different concentrations of AbpG(401-600) showed that the lowest effective concentration was around 5 μM in reactions containing 7.75 μM actin (Supplemental Figure S4B). We measured depolymerization of pyrene-labeled F-actin in the presence of AbpG fragments and found that depolymerization was accelerated slightly by AbpG(501-550) and substantially by AbpG(401-600) but not by AbpG(401-600)Δ501-550 or GST (Figure 7B). Further dose–response analysis found that 2.5 μM AbpG(401-600) still had an effect on in vitro depolymerization reactions containing 7 μM F-actin (Supplemental Figure S4C). These results suggest that AbpG might participate in regulating cellular actin

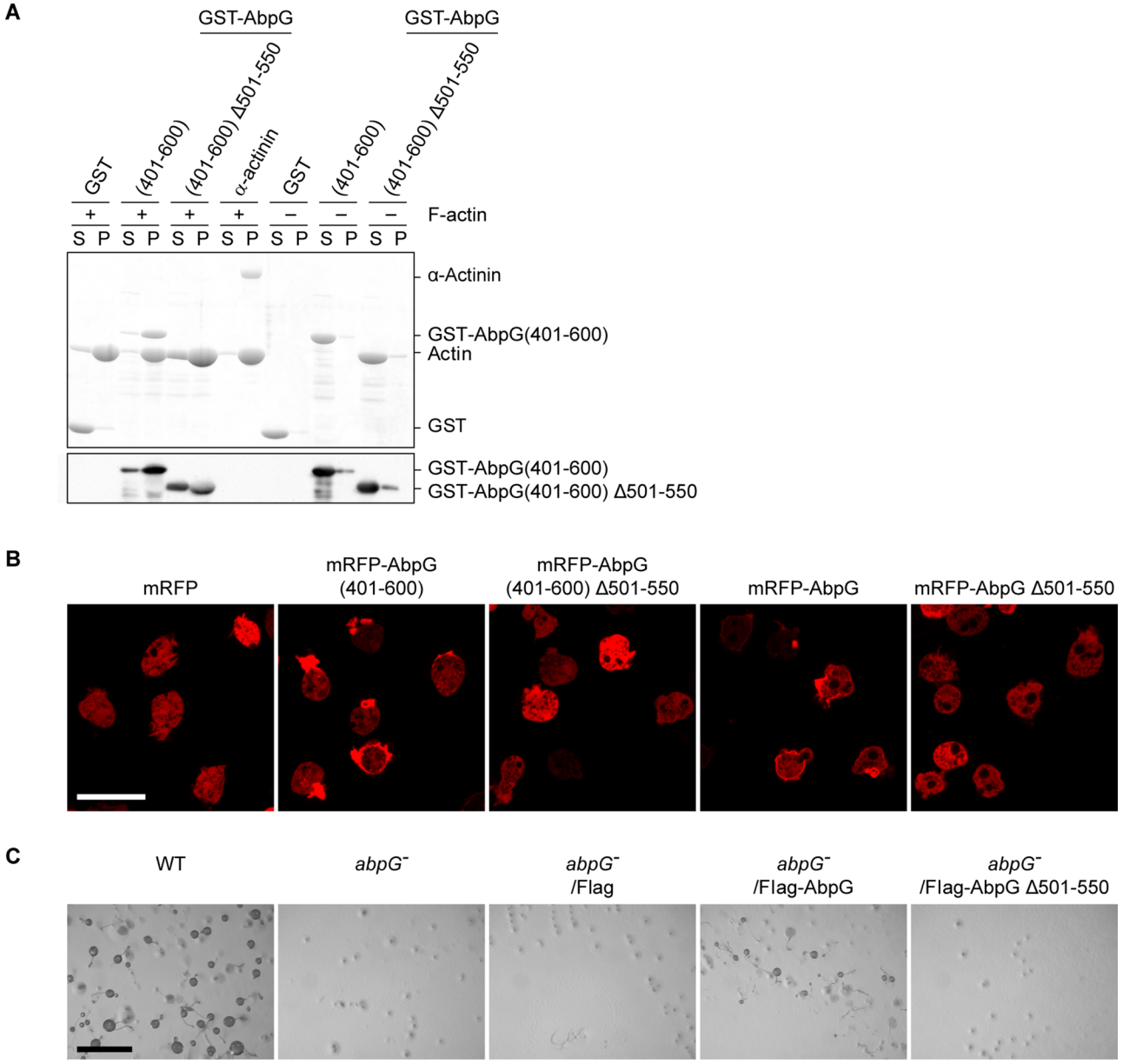

FIGURE 6: Functional significance of the actin-binding region of AbpG. (A) In vitro F-actin sedimentation assay. Recombinant GST-AbpG fragments purified from bacteria were added in the actin polymerization reactions. After sedimentation of F-actin by centrifugation, proteins in supernatant and pellet fractions were analyzed using SDS–PAGE, followed by Coomassie blue staining (top) or Western blotting (bottom). Western blotting was used to detect GST-AbpG(401-600)Δ501-550 because its molecular weight is similar to that of actin. (B) Live-cell images. Live vegetative wild-type cells expressing different mRFP-AbpG fragments were observed under a confocal microscope. Bar, 20 μm. (C) Developmental phenotype. Cells were developed on bacterial lawns. Photographs were taken 5–7 d after plating. Bar, 2 mm.

dynamics by inhibiting polymerization and/or promoting depolymerization to decrease the level of F-actin; the data also demonstrated that the regulatory function of AbpG requires its actin-binding domain. Given the aforementioned finding that AbpG(401-600) can directly bind to F-actin, we investigated whether it has capping activity. We tested the effect of AbpG(401-600) on the kinetics of in vitro actin polymerization in assays performed for an extended reaction time. The results show that AbpG(401-600) both inhibited the rate of polymerization and affected the final level of F-actin formed (Supplemental Figure S4D), suggesting that AbpG(401-600) may possess some capping activity.

We next examined the actin cytoskeleton in *abpG*⁻ cells. We transformed a plasmid to express LifeAct-GFP, a GFP-fused peptide that specifically binds to F-actin but does not interfere with actin dynamics (Riedl *et al.*, 2008), into wild-type and *abpG*⁻ cells and compared their F-actin distributions when cells were migrating under cAMP stimulation. The results demonstrated that the LifeAct-GFP signals could similarly localize to the leading edge in both wild-type and mutant cells (Figure 7C and Supplemental Movies S10 and S11). When the cAMP-induced F-actin polymerization response was investigated by examining the amount of actin in the Triton-insoluble cytoskeleton fraction, the results showed that F-actin levels in

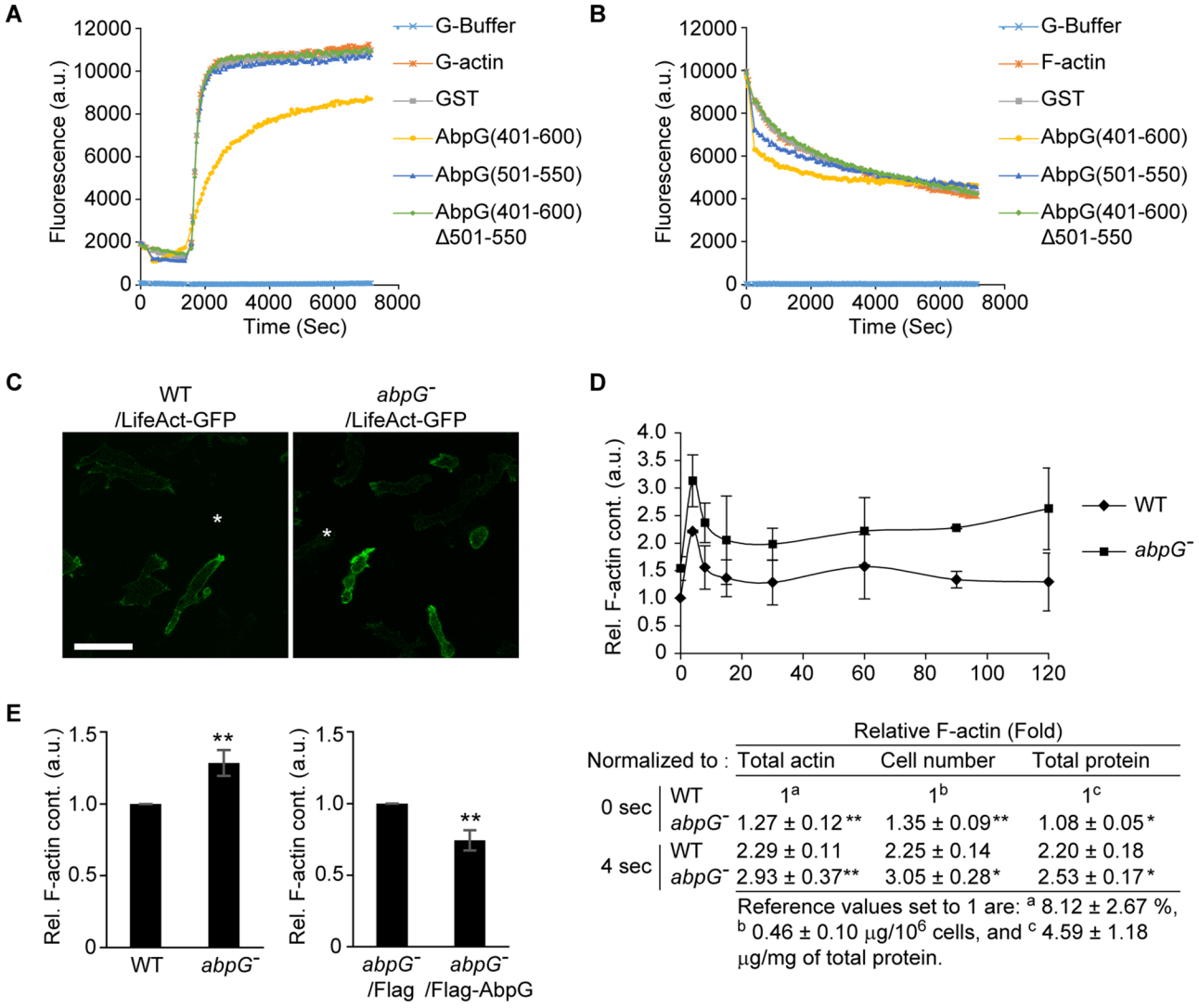

Normalized to :		Relative F-actin (Fold) Total actin	Cell number	Total protein
0 sec	WT	1[a]	1[b]	1[c]
	abpG⁻	1.27 ± 0.12**	1.35 ± 0.09**	1.08 ± 0.05*
4 sec	WT	2.29 ± 0.11	2.25 ± 0.14	2.20 ± 0.18
	abpG⁻	2.93 ± 0.37**	3.05 ± 0.28*	2.53 ± 0.17*

Reference values set to 1 are: [a] 8.12 ± 2.67 %, [b] 0.46 ± 0.10 μg/10^6 cells, and [c] 4.59 ± 1.18 μg/mg of total protein.

FIGURE 7: The role of AbpG in actin dynamics. (A) In vitro actin polymerization. Pyrene-labeled actin monomers (7.75 μM) were used in polymerization reactions. Recombinant test proteins (10 μM) were added into the reactions at 300 s. Fluorescence was monitored for 2 h using a fluorescence reader. (B) In vitro F-actin depolymerization. Recombinant test proteins (5 μM) were added to preformed pyrene-labeled F-actin (7 μM) at 180 s, and the fluorescence was monitored for 2 h. (C) F-actin distribution in migrating cells. Wild-type or *abpG*⁻ cells expressing LifeAct-GFP were developed on non-nutrient agar and subjected to the micropipette chemotaxis assay. The distribution of green fluorescence was observed under a confocal microscope. Asterisk shows the position of the Femtotip. Bar, 20 μm. (D) cAMP-stimulated actin polymerization. Cells developed for 5–6 h were stimulated with 10^{-4} M cAMP at time 0 and sampled at indicated time points into a Triton X-100–containing lysis buffer. The input lysates and detergent-insoluble cytoskeleton fractions were prepared and analyzed using SDS–PAGE, followed by Coomassie blue staining. The intensities of actin protein bands were analyzed by Multi Gauge software, and relative F-actin content normalized to the total actin amount in input lysate was calculated for each time point. Shown are relative F-actin contents (mean ± SD) compared with the wild-type time 0 sample (which is set to 1) obtained from three independent experiments. Shown below the plot are fold values of F-actin content (relative to the value of time 0 wild-type sample, which is set to 1) calculated by using three different normalization standards, including the total actin amount, the cell number, and the total protein amount in the input lysate. *$p < 0.05$, **$p < 0.01$ (comparing corresponding wild-type and *abpG*⁻ samples). (E) Phalloidin binding assay. Aggregation-competent cells were lysed in a buffer containing Phalloidin-TRITC, and the level of F-actin was measured by detecting the fluorescence intensity of the pellet. Shown are relative F-actin content (mean ± SD) obtained from three independent experiments. **$p < 0.01$.

abpG⁻ cells appeared to be higher than those in wild-type cells (Figure 7D); however, the kinetics of response was similar in wild-type and *abpG*⁻ cells (Supplemental Figure S4E). We calculated the relative F-actin levels by normalizing to the total actin amount, the cell number, or the total protein amount in the input lysates, and all three calculations showed higher relative F-actin contents in samples from *abpG*⁻ cells than in corresponding wild-type samples (Figure 7D). We used another method, with a fluorescent phalloidin conjugate to measure cellular F-actin contents, and confirmed that the F-actin level in *abpG*⁻ cells was significantly higher than that in wild-type cells; expression of Flag-AbpG was able to lower the F-actin level in *abpG*⁻ cells (Figure 7E). Together these data suggest that AbpG may participate in modulating actin dynamics and cellular F-actin contents.

DISCUSSION

Functional domains of AbpG

In this study, we identified *Dictyostelium* AbpG as a novel actin-binding protein that serves to support optimal cell migration. Although AbpG contains a CH domain in its N-terminal region, our results defined another region, aa 501–550, as its actin-binding domain. The sequence of AbpG aa 501–550 does not show significant homology to any known actin-binding motifs in databases, indicating that this is a novel protein domain for actin interaction.

Besides the 50-aa actin interaction region, the functional domains of AbpG have not been fully defined. The CH domain, with a sequence of ~100 aa, was first identified in calponin, and subsequently different types of CH domain were found in various cytoskeletal and signal transduction proteins (Korenbaum and Rivero, 2002). The well-known actin-binding domain (ABD) contains CH1 and CH2 domains in tandem. The CH1 domain is able to interact with F-actin, whereas the CH2 domain in ABD can promote the binding of CH1 with F-actin; it is believed that the CH2 domain alone does not confer actin binding (Gimona *et al.*, 2002). The single CH domain in AbpG is of the CH2 type and therefore may not interact with F-actin. Although we did not directly test the actin-binding activity of this domain, the notion is supported by our finding that the AbpG CH2 domain is neither required nor sufficient for the colocalization with F-actin at lamellipodia. In humans, there are proteins that contain a single CH2 domain, including smoothelin, MICAL, and their related proteins (Korenbaum and Rivero, 2002; Friedberg, 2010). These single-CH2-domain–containing proteins seem to act as scaffold proteins and participate in cytoskeleton-related functions. For example, MICAL-1 interacts with Rab1 and vimentin and functions as a scaffold protein in the regulation of vesicular transport in the ER–Golgi compartment (Weide *et al.*, 2003). MICAL-L2 interacts with Rab13 and can be recruited to cell–cell junctions through its interaction with actinin-4 and play a role in the regulation of tight junctions (Nakatsuji *et al.*, 2008). There are four single-CH2- domain–containing proteins, including AbpG, in *D. discoideum*, and their functions had not been characterized previously (Friedberg and Rivero, 2010). Because AbpG seems to interact with F-actin in a CH2 domain–independent manner, the functional significance of the CH2 domain and whether AbpG also serves a scaffolding function require further investigation.

There are two large coiled-coil domains spanning almost the entire region C-terminal to the CH2 domain in AbpG; according to the Conserved Domain Database (www.ncbi.nlm.nih.gov/cdd/), this region of AbpG is significantly similar to the structural maintenance of chromosomes (SMC) superfamily proteins (Hirano, 2006). Of interest, SMC proteins have a structural organization reminiscent of myosins and kinesins, with N-terminal and C-terminal globular ATP-binding domains and a central region containing two coiled-coiled domains (Peterson, 1994). More structure–function studies are needed to understand the importance of this part of the AbpG protein.

Interaction between AbpG and actin

Various actin-binding motifs found in actin-binding proteins interact with actin differently. The ABD formed by tandem CH domains appears to interact only with F-actin (Korenbaum and Rivero, 2002). The WH2 domains bind to actin monomers (Paunola *et al.*, 2002). The ADF-H and gelsolin homology domains can bind to both G-actin and F-actin (McGough *et al.*, 2003; Poukkula *et al.*, 2011). The colocalization of mRFP-AbpG(501-550) with F-actin at lamellipodia, the pull down of actin from lysates of untreated cells but not lysates from latrunculin B–treated cells by GST-AbpG(501-550), and the cosedimentation of GST-AbpG(501-550) with F-actin in vitro suggest that the aa 501–550 region of AbpG can directly interact with F-actin. Because we were unsuccessful in preparing the recombinant full-length AbpG protein, we were not able to test the direct interaction between F-actin and full-length AbpG in vitro. However, the colocalization of full-length AbpG with F-actin at lamellipodia and the loss of this colocalization when the aa 501–550 region is deleted from the full-length AbpG support the conclusion that AbpG interacts with F-actin through its aa 501–550 region. On the other hand, although results from in vitro G-actin sequestering assays demonstrate that AbpG(401-600) does not sequester G-actin monomers, we cannot exclude the possibility that AbpG interacts with actin monomers, because the full-length protein has not been tested.

Our results are consistent with a scenario in which the interaction of AbpG with F-actin directs AbpG to the lamellipodia. In the series of mRFP-AbpG fragments, all those that display a cortical/lamellipodial distribution contain the aa 501–550 F-actin-binding region. Moreover, deletion of aa 501–550 from the full-length AbpG and the aa 401–600 fragment causes them to lose the lamellipodial localization. Given that the appearance of AbpG and F-actin at lamellipodia of live migrating cells display the same kinetics and that cells with no AbpG expression still exhibit F-actin at lamellipodia, we conclude that the lamellipodial recruitment of AbpG is not a prerequisite for actin polymerization at the leading edge of cells.

The role of AbpG in regulating actin dynamics

Like many other actin-binding proteins in cells, AbpG plays a role in modulating the dynamics of the actin cytoskeleton. In vitro data support that AbpG may bind to F-actin to facilitate depolymerization. Two actin-binding fragments, AbpG(401-600) and AbpG(501-550), are able to accelerate the depolymerization, whereas AbpG(401-600)Δ501-550 (which binds poorly to F-actin) does not have an effect on the reaction. Furthermore, AbpG may also perturb F-actin assembly. AbpG(401-600) can inhibit actin polymerization in vitro, whereas AbpG(501-550) and AbpG(401-600)Δ501-550 have no detectable effects; these results suggest that the aa 501–550 region of AbpG is required, but is not by itself sufficient, for suppressing actin polymerization. Consistent with a conclusion that AbpG inhibits actin polymerization and enhances F-actin depolymerization, F-actin levels in *abpG*$^{-}$ cells are abnormally high. However, AbpG is not required for the chemoattractant receptor/G protein signaling-induced actin polymerization, as *abpG*$^{-}$ cells are still able to show a typical biphasic F-actin assembly response upon cAMP stimulation.

The molecular functions of AbpG for skewing the actin dynamics in favor of G-actin remain to be determined. Although we provide data supporting that AbpG(401-600) may have capping activity, whether the full-length AbpG protein binds to the barbed end to perturb the incorporation of new actin monomers into F-actin has not been investigated. We showed that AbpG(401-600) can accelerate actin depolymerization in vitro. AbpG(401-600) or the full-length AbpG does not display any sequence or structural resemblance to ADF/cofilin proteins, a major class of ABPs for dissembling F-actin (Poukkula *et al.*, 2011); therefore AbpG may represent the first member of a novel class of ABPs involved in promoting F-actin turnover.

The role of AbpG in modulating cell migration

The distribution of AbpG to the leading edge of lamellipodia in migrating cells and the migration defect in cells lacking functional AbpG highlight the pivotal role of AbpG in modulating cell motility.

How does AbpG regulate cell motility? In *abpG*$^-$ cells, the chemoattractant-elicited actin polymerization response still happens, but why is it not sufficient to drive efficient cell migration? Does the excessive F-actin in *abpG*$^-$ cells cause the migration defect? Further investigations are required to answer these questions.

We noticed some interesting similarities in phenotypes of *abpG*$^-$ cells and cells lacking SCAR (*scrA*$^-$ cells) or the SCAR/WAVE complex protein PIR121 (*pirA*$^-$ cells; Blagg *et al.*, 2003; Bastounis *et al.*, 2011): 1) Cells can still move, albeit at lower-than-wild-type speeds; 2) mutants display a less polarized morphology, with decreased length/width ratios compared with that of wild-type cells; 3) in response to the chemoattractant, all three mutants exhibit proportional, stimulus-induced biphasic F-actin polymerization; 4) all three mutants display similar localization of the F-actin reporter LifeAct; 5) all three mutants show reduced substrate adhesion (Supplemental Figure S5); and 6) *abpG*$^-$ and *pirA*$^-$ cells, but not *scrA*$^-$, cells display higher-than-normal F-actin levels. The Arp2/3 complex provides nucleation for actin filament branching, which is important for dendritic polymerization at lamellipodia (Cooper *et al.*, 2001; Beltzner and Pollard, 2008). F-actin nucleation-promoting factors, including WASP and SCAR/WAVE protein complexes, bind and activate the Arp2/3 complex to nucleate for actin filament production in cells (Machesky and Insall, 1998; Blagg and Insall, 2004). Although mutations in these regulators do not prevent F-actin assembly, they may affect the strength of cellular traction stress (which is determined by the amount of F-actin) and the regulation of the motility cycle during migration (Bastounis *et al.*, 2011). Given the similarities of the mutant phenotypes mentioned, there exists an intriguing possibility that AbpG may be functionally linked to WASP and SCAR/WAVE or the Arp2/3 complex. It remains to be elucidated whether AbpG regulates pseudopodial activities by interacting with Arp2/3 and/or SCAR/WAVE.

MATERIALS AND METHODS

Cell growth, development, and transformation

D. discoideum (strain AX-2) cells were grown at 22°C in the HL-5 medium. To examine the developmental morphology, cells were grown on SM plates with *Klebsiella aerogenes* (Sussman, 1987). To prepare aggregation-competent cells, cells were developed by cAMP pulsing or on non-nutrient agar plates. For development by cAMP pulsing, cells were washed and suspended in phosphate buffer (5 mM Na_2HPO_4, 5 mM KH_2PO_4, pH 6.5) at 2×10^7 cells/ml, incubated for 1 h with gentle shaking, and further incubated for 4–5 h with 10^{-7} M cAMP pulses every 6 min (Devreotes *et al.*, 1987). For non-nutrient plate development, (5–8) $\times 10^6$ cells were placed on 10-cm non-nutrient agar plates and harvested when aggregation was observed. For transformation, 4×10^7 cells in 0.8 ml of E buffer (10 mM K_2HPO_4/KH_2PO_4, 50 mM sucrose, pH 6.1) were mixed with 15–25 μg of DNA, and electroporation was done at 900 V/0.3 μF using a Bio-Rad Gene Pulser II. For selection of transformants, cells were cultured in HL-5 medium containing 5 μg/ml blasticidin S (InvivoGen, San Diego, CA), 10 μg/ml G418 (Sigma-Aldrich, St. Louis, MO), or 50 μg/ml hygromycin B (Invitrogen, Carlsbad, CA), depending on the plasmid used.

Cloning of *abpG* and generation of the *abpG*$^-$ mutant

The *abpG* gene was identified by cloning the genomic fragments flanking the REMI insertion site in the T6#16 mutant clone. Genomic DNA from T6#16 was digested with *Bcl*I and subjected to the REMI plasmid recovery procedures previously described (Kuspa and Loomis, 1992). Sequence analysis of the recovered plasmid (pT6#16), which contained a ~5-kb *Bcl*I genomic fragment, located the REMI insertion site within DDB0185522, the open reading frame of *abpG*. We cloned the full-length *abpG* sequence as follows. We performed TA-cloning of 5′ and 3′ fragments of *abpG*, which were amplified from AX-2 cDNA using T6#16-R2/T6#16-antiA primers and from AX-2 genomic DNA using T6#16-R1/T6#16-L3 primers, respectively, into yTA (YEASTERN, Taipei, Taiwan) to obtain yTA-AbpG-5′region and yTA-AbpG-3′region. The *Sac*I-*Cla*I *abpG* fragment from yTA-AbpG-5′region was subcloned into *Sac*I/*Cla*I-digested yTA-AbpG-3′region, generating the full-length *abpG*-containing yTA-T6#16 plasmid. The pTX-Flag-AbpG plasmid for expression of AbpG with an N-terminal Flag tag was generated by ligating the *Sac*I-*Xho*I full-length *abpG* fragment from yTA-T6#16 to *Sac*I/*Sal*I-digested pTX-Flag (Levi *et al.*, 2000). All oligonucleotide primers used in this study are listed in Supplemental Table S1.

The *abpG*$^-$ mutant was generated as follows. A 2806–base pair *abpG* genomic fragment amplified by PCR using T6#16-R2 and T6#16-L2 primers was subcloned into pGEM-T (Promega, Fitchburg, WI) to generate pGEM-T6#16. An *Eco*RI-*Hin*dIII fragment from pPTGalΔBglII (a gift from W.-T. Chang, National Cheng-Kung University, Tainan City, Taiwan) containing an expression cassette for the blasticidin S resistance (*Bsr*) gene was subcloned into *Eco*RI/*Hin*dIII-digested pGEM-T6#16 to generate the pGEM-6#16::Bsr plasmid. The *Bsr*-containing *Nco*I-*Sal*I fragment from pGEM-6#16::Bsr was transformed into wild-type cells, and transformants were selected in the blasticidin S–containing medium. Genomic DNA from candidate clones was subjected to genotype analysis by PCR and Southern blotting to identify the knockout clones.

Antibodies

Polyclonal antibodies against N-terminal aa 1–152, C-terminal aa 845–919, and aa 401–600 regions of AbpG were generated as follows. The nucleotide 1–458, 2533–2757, and 1201–1800 regions of *abpG* coding sequence were amplified by PCR using primer sets T6#16-ab1-F /T6#16-ab1-R, T6#16-ab2-F/T6#16-ab2-R, and AbpG-1201-F/AbpG-1800-R, respectively, and subcloned into yTA. The *Eco*RI/*Xho*I-digested N-terminal and C-terminal fragments were subcloned into *Eco*RI/*Xho*I-digested pGEX-5X-3, and the *Bam*HI-digested AbpG(401-600)-coding fragment was ligated into *Bam*HI-digested pGEX-4T-2 to generate pGEX-5X-3-ab1#3, pGEX-5X-3-ab2#12, and pGEX-4T-2-AbpG(401-600). *E. coli* strain BL21(DE3) was transformed with pGEX-5X-3-ab1#3, pGEX-5X-3-ab2#12, or pGEX-4T-2-AbpG(401-600) and induced by 0.5 mM isopropyl-1-thio-β-d-galactopyranoside (BioShop, Burlington, ON, Canada) for 3–6 h to express GST-AbpG fragment fusion proteins. GST-AbpG fusion proteins were purified using glutathione Sepharose beads (GE Healthcare, Uppsala, Sweden) following the manufacturer's protocol. The purified proteins were mixed with TiterMax Gold adjuvant (Sigma-Aldrich) and used to immunize female New Zealand white rabbits.

Antibodies against GST were affinity purified from antisera produced by rabbits immunized with GST-AbpG(1-152). A goat polyclonal anti-actin antibody (I-19; Santa Cruz Biotechnology, Dallas, TX) was used to detect actin.

Chemotaxis assays

The small-drop assay was performed as previously described (Konijn and Van Haastert, 1987). Briefly, cells were developed for 5–6 h with cAMP pulsing to become aggregation competent. Harvested cells were incubated in a buffer containing 3 mM caffeine (Sigma-Aldrich) for 25 min. On 1.5% non-nutrient agar containing 3 mM caffeine, small drops of cell suspension were each placed adjacent to a drop

of cAMP; >10 pairs of cell and cAMP drops were set up for each cAMP concentration in each experiment. After incubation for 20 min, cell-containing drops were examined under an inverted microscope (Axiovert S100; Zeiss, Oberkochen, Germany). Drops displaying asymmetrical cell distribution with more cells on the side of the cAMP source were scored positive. For each cAMP concentration, the percentage of positive drops was calculated and used as a score for chemotaxis.

The micropipette chemotaxis assay was performed as previously described (Pang *et al.*, 2010). A 50-µl aliquot of 4×10^5 aggregation-competent cells was placed in a 3.5-cm culture dish. Cells were allowed to stand for 10 min before the dish was filled with 5 ml of phosphate buffer. A Femtotip (Eppendorf, Hamburg, Germany) containing 10^{-4} M cAMP was placed in the center of the field, and cAMP was released using a pressure of 40 hPa. On cAMP stimulation, images of cells were recorded under an inverted microscope (DMIRBE; Leica Microsystems, Wetzlar, Germany) equipped with a 10× objective lens (N PLAN, numerical aperture [NA] 0.25) every 10 s for 20 min using a charge-coupled device camera (CoolSNAP; Photometrics, Tucson, AZ).

Computer-assisted image analysis

For analysis of the behavior of individual migrating cells, images captured in micropipette chemotaxis assays were analyzed using MetaMorph software (Molecular Devices, Sunnyvale, CA). Three independent experiments were done, and for each strain, 30 cells were randomly selected for image analysis. The centroid of each cell was traced. Migration speed was the average displacement of cell centroid per minute determined by tracing the total distance traveled in 20 min. Directional persistence was the ratio of net path length to total path length. Chemotaxis index was the mean cosine value of the angle between the line depicting the direction of movement and the line formed by the initial centroid position and the Femtotip.

For analysis of cell shape during directional migration, GFP-expressing cells were developed on non-nutrient agar until aggregation began. Cells were harvested, plated on 3.5-cm FluoroDish (WPI, Sarasota, FL), and subjected to the micropipette chemotaxis assay and observed under a confocal fluorescence microscope (TCS SP5; Leica) with a 100× objective (HCX PL APO, NA 1.4). Images were captured every 4 s and analyzed using MetaMorph software. To calculate the length/width ratio of a cell, a line was drawn through the cell body to bisect the cell along its longest axis for the measurement of "length," and a perpendicular line was drawn at the midpoint of this line for the measurement of "width." For each cell, the average length/width ratio was calculated using 30 images from the same cell, and 26 wild-type and 16 *abpG*$^-$ GFP-expressing cells from three independent experiments were analyzed.

For analysis of dynamic protein distribution during directional migration, cells simultaneously expressing mRFP-AbpG and LifeAct-GFP were prepared. The plasmid for expressing mRFP-AbpG was generated; a *Bam*HI cutting site was engineered 5′ to the full-length *abpG* coding sequence by PCR to produce yTA-AbpG-pdm, and the *abpG*-containing *Bam*HI fragment from yTA-AbpG-pdm was subcloned into *Bgl*II-digested pDM358-mRFPmars (Veltman *et al.*, 2009), resulting in pDM358-mRFPmars-AbpG. The plasmid to express LifeAct-GFP in *Dictyostelium* cells was generated as follows. A *GFP* fragment was amplified by PCR from pDM313 (Veltman *et al.*, 2009) using TagGFP-F1 and TagGFP-R1 primers and subcloned into yTA to generate yTA-GFP. The *RFP* region of pCMVLifeAct-TagRFP (ibidi, Martinsried, Germany) was replaced with the *Bam*HI-*Xba*I *GFP* fragment from yTA-GFP to generate pCMVLifeAct-GFP. Finally, the *Bgl*II-*Xba*I LifeAct-GFP fragment from pCMVLifeAct-GFP was subcloned into *Bgl*II/*Spe*I-digested pDM304 (Veltman *et al.*, 2009) to generate pDM304-LifeAct-GFP. To compare the kinetics of the enrichment of AbpG and F-actin at lamellipodia during cell migration, wild-type cells cotransformed with pDM358-mRFPmars-AbpG and pDM304-LifeAct-GFP were developed and subjected to micropipette chemotaxis analysis and time-lapse fluorescence video microscopy as in the aforementioned cell-shape analysis. The appearance of mRFP-AbpG and LifeAct-GFP signals at lamellipodia was analyzed by quantifying the fluorescence intensities in a fixed square area at the lamellipodial front. The values obtained from fluorescence quantitation were further adjusted by subtracting away values representing the average background mRFP or GFP fluorescence, and the adjusted values were plotted against time.

Preparation of the detergent-insoluble cytoskeleton

Detergent-insoluble cytoskeleton was prepared as described previously (Wang *et al.*, 2011). Briefly, aggregation-competent cells were lysed in Triton X-100 buffer (10 mM KCl, 10 mM imidazole, 50 µg/ml NaN_3, 1% Triton X-100, 10 mM ethylene glycol tetraacetic acid [EGTA], and protease inhibitors) on ice for 10 min. Lysates were further incubated at room temperature for 10 min, and samples containing equal protein amounts were centrifuged at 8000 × *g* for 4 min. The supernatant was collected, and the pellet was washed once with Triton X-100 buffer and resuspended in SDS sample buffer. Supernatant and pellet samples were analyzed by SDS–PAGE and Western blotting.

Fluorescence cell staining

For examining the localization of AbpG in cells, Flag-AbpG–expressing vegetative- or aggregative-stage cells were fixed in 3.7% formaldehyde in phosphate buffer (5 mM Na_2HPO_4, 5 mM KH_2PO_4, pH 6.5), washed with phosphate-buffered saline (PBS; 137 mM NaCl, 2.7 mM KCl, 10 mM Na_2HPO_4, 1.8 mM KH_2PO_4, pH 7.4), and permeabilized in 0.2% Triton X-100 in PBS. After blocking with 10% fetal bovine serum, cells were washed with PBS for three times and reacted with tetramethylrhodamine B isothiocyanate (TRITC)–conjugated phalloidin (Phalloidin-TRITC; Sigma-Aldrich) and purified anti-AbpG(1-152) antibodies plus fluorescein isothiocyanate (FITC)–conjugated goat anti-rabbit antibodies for detection. Fluorescence signals were observed by confocal microscopy using a Leica microscope (TCS SP5) with a 100× objective (HCX PL APO, NA 1.4) or a Zeiss microscope (LSM700) with a 100× objective (Plan-Apochromat, NA 1.4, oil).

Mapping the protein region for lamellipodial localization of AbpG

Plasmids for expressing different mRFP-fused AbpG fragments were generated as follows. DNA fragments coding for specific AbpG regions were obtained by PCR amplification from yTA-AbpG-pdm, subcloned into yTA, and subsequently moved as *Bam*HI-digested fragments from yTA derivatives into *Bgl*II-digested pDM358-mRFPmars to generate each pDM358-mRFPmars-AbpG(fragment). Primers used in PCR are listed in Supplemental Table S1.

Wild-type cells were transformed with individual mRFP-AbpG fragment–expressing constructs. Live vegetative cells in 3.5-cm FluoroDish (WPI) were observed under a confocal microscope (TCS SP5) with a 100× objective (HCX PL APO, NA 1.4). For examining the colocalization of mRFP-AbpG fragments and F-actin, wild-type cells expressing different mRFP-AbpG fragments were developed, fixed, and permeabilized as before. After staining with FITC-labeled phalloidin (Phalloidin-FITC), images were taken under a confocal

fluorescence microscope (LSM700) with a 100× objective (Plan-Apochromat, NA 1.4, oil).

Immunoprecipitation

Wild-type or *abpG*$^{-}$ cells transformed with the Flag control vector or Flag-AbpG–expressing plasmid were developed to the aggregation stage. Lysates were prepared and incubated with Anti-Flag M2 affinity gel (Sigma-Aldrich). After three washes with lysis buffer, proteins adhered on the affinity gel were analyzed by SDS–PAGE and Western blotting.

GST pull-down assay

Plasmids for expressing different GST-fused AbpG fragments in *Dictyostelium* or *E. coli* were generated as follows. DNA fragments of different regions of *abpG* were amplified from yTA-AbpG-pdm by PCR using primers listed in Supplemental Table S1. PCR products were subcloned into yTA and subsequently moved as *Bam*HI-digested fragments from yTA derivatives into *Bgl*II-digested pDM314 or *Bam*HI-digested pGEX-4T-2 to generate each pDM314-AbpG(fragment) or pGEX-4T-2-AbpG(fragment). To test the interaction of AbpG with F-actin, *Dictyostelium* cells transformed with pDM314-AbpG(fragment) were developed to the aggregative stage, and lysates were prepared for GST pull-down assays. Alternatively, GST-fusion proteins were expressed in the BL21 strain of *E. coli*, purified, and mixed with lysates of aggregation-competent wild-type *Dictyostelium* cells. Pull down was performed using glutathione Sepharose beads. After three washes in lysis buffer (40 mM sodium pyrophosphate, 0.4 mM dithiothreitol, 0.1 mg/ml phenylmethylsulfonyl fluoride, 2 mM EDTA, 1 mM EGTA, 3 mM sodium azide, 0.5% NP-40, 1% protease inhibitor, 10 mM Tris-HCl, pH 7.6), proteins adhered on glutathione Sepharose beads were analyzed using SDS–PAGE, followed by Western blotting. For latrunculin B treatment, aggregative-stage wild-type *Dictyostelium* cells were incubated for 20 min with 60 μM latrunculin B (Sigma-Aldrich) or dimethyl sulfoxide (Sigma-Aldrich) as a control.

Actin assays

The in vitro F-actin sedimentation assay was performed with the Actin Binding Protein Spin Down Assay (nonmuscle) kit (BK013; Cytoskeleton, Denver, CO). Briefly, recombinant proteins (60 μM) purified from *E. coli* or α-actinin were mixed with polymerized nonmuscle actin (21 μM) and incubated for 30 min at 22°C. The mixtures were centrifuged to sediment F-actin, and the supernatant and pellet fractions were analyzed using SDS–PAGE, followed by Coomassie blue staining.

In vitro actin polymerization and depolymerization assays were performed using the Actin Polymerization Biochem Kit (BK003; Cytoskeleton). Test proteins used in these assays were prepared as follows. GST-AbpG fragments expressed in *E. coli* were purified using glutathione Sepharose beads. The GST part from fusion proteins was removed by incubating the purified fusion proteins with thrombin beads (Sigma-Aldrich) and subsequently with glutathione Sepharose beads. For the actin polymerization assay, the test protein was added into 7.75 μM pyrene G-actin in G-buffer to a concentration of 10 μM. For the F-actin depolymerization assay, 7 μM preformed pyrene F-actin in G-buffer was mixed with 5 μM test protein. For both assays, fluorescence was monitored by a fluorescence reader (Infinite M200; Tecan, Männedorf, Switzerland) at room temperature.

To assay cAMP-stimulated actin polymerization, developed cells were incubated in phosphate buffer containing 3 mM caffeine (Sigma-Aldrich) for 25 min and subsequently stimulated by 10 μM cAMP. Aliquots were sampled before (time 0) and at time points after cAMP stimulation and immediately mixed with equal volume of 2× Triton X-100 buffer to prepare the detergent-insoluble cytoskeleton fraction. The cytoskeleton pellets were resuspended in SDS sample buffer and analyzed along with bovine serum albumin (BSA) samples of known protein amounts by SDS–PAGE. Protein bands of actin and BSA in samples were visualized by Coomassie brilliant blue staining and quantified using the Multi Gauge software (Fujifilm, Tokyo, Japan). The actual level of actin in each sample was calculated by comparing with the BSA standards.

To measure the relative F-actin content of cells, a phalloidin binding assay was performed as previously described (Insall *et al.*, 1996). Briefly, cells developed by cAMP pulsing for 5–6 h were harvested and incubated in phosphate buffer containing 3 mM caffeine (Sigma-Aldrich) for 25 min. Cells (3×10^6) were suspended in 1 ml of assay buffer (20 mM KPO_4, 10 mM 1,4-piperazinediethanesulfonic acid, 5 mM EGTA, 4 mM $MgCl_2$, 0.1% Triton X-100, 3.7% formaldehyde) containing 250 nM Phalloidin-TRITC and incubated at 22°C for 1 h. Samples were centrifuged at 14,000 rpm in a microfuge at 22°C for 10 min, and the pellets were extracted with methanol overnight. Fluorescence intensity in the extract was measured by a fluorescence reader (Infinite M200).

ACKNOWLEDGMENTS

We thank Min-Lun Li for critical reading of the manuscript. This work was supported by Grant NHRI-EX94-9230SI from the National Health Research Institutes, Taiwan, and Grant Aim for the Top University Plan 103AC-T307 from the Ministry of Education, Taiwan.

REFERENCES

Bastounis E, Meili R, Alonso-Latorre B, del Alamo JC, Lasheras JC, Firtel RA (2011). The SCAR/WAVE complex is necessary for proper regulation of traction stresses during amoeboid motility. Mol Biol Cell 22, 3995–4003.

Beltzner CC, Pollard TD (2008). Pathway of actin filament branch formation by Arp2/3 complex. J Biol Chem 283, 7135–7144.

Bisi S, Disanza A, Malinverno C, Frittoli E, Palamidessi A, Scita G (2013). Membrane and actin dynamics interplay at lamellipodia leading edge. Curr Opin Cell Biol 25, 565–573.

Blagg SL, Insall RH (2004). Control of SCAR activity in Dictyostelium discoideum. Biochem Soc Trans 32, 1113–1114.

Blagg SL, Stewart M, Sambles C, Insall RH (2003). PIR121 regulates pseudopod dynamics and SCAR activity in Dictyostelium. Curr Biol 13, 1480–1487.

Bravo-Cordero JJ, Hodgson L, Condeelis J (2012). Directed cell invasion and migration during metastasis. Curr Opin Cell Biol 24, 277–283.

Cooper JA, Wear MA, Weaver AM (2001). Arp2/3 complex: advances on the inner workings of a molecular machine. Cell 107, 703–705.

Cramer LP (2013). Mechanism of cell rear retraction in migrating cells. Curr Opin Cell Biol 25, 591–599.

Devreotes P, Fontana D, Klein P, Sherring J, Theibert A (1987). Transmembrane signaling in Dictyostelium. Methods Cell Biol 28, 299–331.

Disanza A, Steffen A, Hertzog M, Frittoli E, Rottner K, Scita G (2005). Actin polymerization machinery: the finish line of signaling networks, the starting point of cellular movement. Cell Mol Life Sci 62, 955–970.

Egelhoff TT, Spudich JA (1991). Molecular genetics of cell migration: Dictyostelium as a model system. Trends Genet 7, 161–166.

Friedberg F (2010). Singlet CH domain containing human multidomain proteins: an inventory. Mol Biol Rep 37, 1531–1539.

Friedberg F, Rivero F (2010). Single and multiple CH (calponin homology) domain containing multidomain proteins in Dictyostelium discoideum: an inventory. Mol Biol Rep 37, 2853–2862.

Funamoto S, Meili R, Lee S, Parry L, Firtel RA (2002). Spatial and temporal regulation of 3-phosphoinositides by PI 3-kinase and PTEN mediates chemotaxis. Cell 109, 611–623.

Gimona M, Djinovic-Carugo K, Kranewitter WJ, Winder SJ (2002). Functional plasticity of CH domains. FEBS Lett 513, 98–106.

Hartman MA, Spudich JA (2012). The myosin superfamily at a glance. J Cell Sci 125, 1627–1632.
Hirano T (2006). At the heart of the chromosome: SMC proteins in action. Nat Rev Mol Cell Biol 7, 311–322.
Insall R (2013). The interaction between pseudopods and extracellular signalling during chemotaxis and directed migration. Curr Opin Cell Biol 25, 526–531.
Insall RH, Borleis J, Devreotes PN (1996). The aimless RasGEF is required for processing of chemotactic signals through G-protein-coupled receptors in Dictyostelium. Curr Biol 6, 719–729.
Insall R, Kuspa A, Lilly PJ, Shaulsky G, Levin LR, Loomis WF, Devreotes P (1994). CRAC, a cytosolic protein containing a pleckstrin homology domain, is required for receptor and G protein-mediated activation of adenylyl cyclase in Dictyostelium. J Cell Biol 126, 1537–1545.
Kay RR (2002). Chemotaxis and cell differentiation in Dictyostelium. Curr Opin Microbiol 5, 575–579.
Kolaczkowska E, Kubes P (2013). Neutrophil recruitment and function in health and inflammation. Nat Rev Immunol 13, 159–175.
Konijn TM, Van Haastert PJ (1987). Measurement of chemotaxis in Dictyostelium. Methods Cell Biol 28, 283–298.
Korenbaum E, Rivero F (2002). Calponin homology domains at a glance. J Cell Sci 115, 3543–3545.
Kuspa A, Loomis WF (1992). Tagging developmental genes in Dictyostelium by restriction enzyme-mediated integration of plasmid DNA. Proc Natl Acad Sci USA 89, 8803–8807.
Lauffenburger DA, Horwitz AF (1996). Cell migration: a physically integrated molecular process. Cell 84, 359–369.
Levi S, Polyakov M, Egelhoff TT (2000). Green fluorescent protein and epitope tag fusion vectors for Dictyostelium discoideum. Plasmid 44, 231–238.
Machesky LM, Insall RH (1998). Scar1 and the related Wiskott-Aldrich syndrome protein, WASP, regulate the actin cytoskeleton through the Arp2/3 complex. Curr Biol 8, 1347–1356.
Machesky LM, Reeves E, Wientjes F, Mattheyse FJ, Grogan A, Totty NF, Burlingame AL, Hsuan JJ, Segal AW (1997). Mammalian actin-related protein 2/3 complex localizes to regions of lamellipodial protrusion and is composed of evolutionarily conserved proteins. Biochem J 328, 105–112.
Maruthamuthu V, Aratyn-Schaus Y, Gardel ML (2010). Conserved F-actin dynamics and force transmission at cell adhesions. Curr Opin Cell Biol 22, 583–588.
McGough AM, Staiger CJ, Min JK, Simonetti KD (2003). The gelsolin family of actin regulatory proteins: modular structures, versatile functions. FEBS Lett 552, 75–81.
Nakatsuji H, Nishimura N, Yamamura R, Kanayama HO, Sasaki T (2008). Involvement of actinin-4 in the recruitment of JRAB/MICAL-L2 to cell-cell junctions and the formation of functional tight junctions. Mol Cell Biol 28, 3324–3335.
Noegel AA, Schleicher M (2000). The actin cytoskeleton of Dictyostelium: a story told by mutants. J Cell Sci 113, 759–766.
Pang TL, Chen FC, Weng YL, Liao HC, Yi YH, Ho CL, Lin CH, Chen MY (2010). Costars, a Dictyostelium protein similar to the C-terminal domain of STARS, regulates the actin cytoskeleton and motility. J Cell Sci 123, 3745–3755.
Paunola E, Mattila PK, Lappalainen P (2002). WH2 domain: a small, versatile adapter for actin monomers. FEBS Lett 513, 92–97.
Peterson CL (1994). The SMC family: novel motor proteins for chromosome condensation? Cell 79, 389–392.
Pollard TD, Borisy GG (2003). Cellular motility driven by assembly and disassembly of actin filaments. Cell 112, 453–465.
Poukkula M, Kremneva E, Serlachius M, Lappalainen P (2011). Actin-depolymerizing factor homology domain: a conserved fold performing diverse roles in cytoskeletal dynamics. Cytoskeleton 68, 471–490.
Prochniewicz E, Janson N, Thomas DD, De la Cruz EM (2005). Cofilin increases the torsional flexibility and dynamics of actin filaments. J Mol Biol 353, 990–1000.
Riedl J, Crevenna AH, Kessenbrock K, Yu JH, Neukirchen D, Bista M, Bradke F, Jenne D, Holak TA, Werb Z, *et al.* (2008). Lifeact: a versatile marker to visualize F-actin. Nat Methods 5, 605–607.
Schultz J, Milpetz F, Bork P, Ponting CP (1998). SMART, a simple modular architecture research tool: identification of signaling domains. Proc Natl Acad Sci USA 95, 5857–5864.
Solnica-Krezel L, Sepich DS (2012). Gastrulation: making and shaping germ layers. Annu Rev Cell Dev Biol 28, 687–717.
Sussman M (1987). Cultivation and synchronous morphogenesis of Dictyostelium under controlled experimental conditions. Methods Cell Biol 28, 9–29.
Veltman DM, Akar G, Bosgraaf L, Van Haastert PJ (2009). A new set of small, extrachromosomal expression vectors for Dictyostelium discoideum. Plasmid 61, 110–118.
Wang Y, Steimle PA, Ren Y, Ross CA, Robinson DN, Egelhoff TT, Sesaki H, Iijima M (2011). Dictyostelium huntingtin controls chemotaxis and cytokinesis through the regulation of myosin II phosphorylation. Mol Biol Cell 22, 2270–2281.
Weide T, Teuber J, Bayer M, Barnekow A (2003). MICAL-1 isoforms, novel rab1 interacting proteins. Biochem Biophys Res Commun 306, 79–86.
Weijer CJ (2009). Collective cell migration in development. J Cell Sci 122, 3215–3223.
Winder SJ, Ayscough KR (2005). Actin-binding proteins. J Cell Sci 118, 651–654.